Nanoscale

PAPER

View Article Online
View Journal | View Issue

Check for updates

Cite this: *Nanoscale*, 2026, **18**, 6542

High surface area mixed lanthanum nickelate/ferrates ($LaNi_{1-x}Fe_xO_3$) *via* modified carbon templating coated on nickel in alkaline OER

Nikolas Mao Kubo, [a] Harol Moreno Fernández, [b] Ilias Efthimiopoulos, [c] Leila Novalic,[a] Martin Rabe, [c] Jan P. Hofmann [b] and Regina Palkovits *[a,d]

Perovskites have been proven as a highly versatile, tailorable material class, encompassing well-established, highly active oxygen evolution reaction (OER) electrocatalysts based on earth-abundant transition metals. Facile synthesis methods yielding large specific surface areas (SSA) for enhanced catalyst utilization and testing in industrially relevant conditions are crucial for accelerating the large-scale application of alkaline OER, which is regarded as a bottleneck for electrocatalytic water splitting. The synthesis of such perovskites with high SSAs, however, remains challenging. Here, a modified carbon templating method, where metal nitrates are impregnated into activated carbon and subsequently precipitated with an additional KOH impregnation step, is applied to synthesize a solid solution series of lanthanum nickelate/ferrate $LaNi_{1-x}Fe_xO_3$ perovskite phases. These materials are tested in the alkaline OER as catalyst coatings applied on Ni metal substrates. XRD analysis confirms the formation of perovskites as primary phases, with SEM, elemental analysis, XPS, and Raman spectroscopy substantiating the material characterization. SSAs determined by N_2 physisorption outperform those prepared by comparably facile syntheses. SEM images reveal a less dense coating of $LaFeO_3$ than $LaNiO_3$ on Ni substrates, positively affecting the OER activity of higher Fe-content catalysts. The stability of the perovskite-coated electrodes is assessed by XPS and Raman spectroscopy before and after chronopotentiometry, recorded for 24 hours.

Received 26th November 2025,
Accepted 12th February 2026

DOI: 10.1039/d5nr05003k

rsc.li/nanoscale

Open Access Article. Published on 25 February 2026. Downloaded on 4/22/2026 8:06:35 AM.
This article is licensed under a Creative Commons Attribution 3.0 Unported Licence.

Introduction

In the transition away from fossil fuel dependency, hydrogen plays a pivotal role as a chemical energy carrier, offering a solution to the intermittency of renewable energy sources and enabling applications as a chemical feedstock in a potential hydrogen economy.[1–7] When powered by renewable energy, the electrolysis of water (electrochemical water splitting, eqn (1)) enables an emission-free and sustainable generation of hydrogen.[7–11]

$$2H_2O \rightarrow 2H_2 + O_2 \quad (1)$$

Water splitting can be conducted at high temperatures in solid oxide electrolysis cells using steam or at near-ambient temperatures in acidic or alkaline aqueous systems with proton exchange membrane (PEM) cells or alkaline water electrolyzers (AWE).[11–15] Generally, water splitting involves two half-cell reactions where hydrogen is obtained in the reduction of water at the cathode (hydrogen evolution reaction) while the oxidation towards oxygen (oxygen evolution reaction, OER) occurs at the anode. As resistances need to be overcome and both half-cell reactions require overpotentials to occur, higher potentials than that of the equilibrium potential of 1.23 V need to be applied in praxis. Here, the OER contributes the largest share to the total overpotential due to its sluggish kinetics resulting from the thermodynamically challenging four-electron transfer and the oxygen–oxygen bond formation.[15–18] Hence, the OER poses a bottleneck to the overall water-splitting technology and is shown in eqn (2) for alkaline media with hydroxyl anions as the main charge carrier.

$$4OH^- \rightarrow O_2 + 2H_2O + 4e^- \quad (2)$$

Although noble-metal-based catalysts such as iridium and ruthenium oxides are highly active and now well-established

[a]*Institute of Technical and Macromolecular Chemistry, RWTH Aachen University, Worringerweg 2, 52074 Aachen, Germany. E-mail: palkovits@itmc.rwth-aachen.de*
[b]*Surface Science Laboratory, Department of Materials and Geosciences, Surface Science Laboratory, Technical University of Darmstadt, Peter-Grünberg-Strasse 4, 64287 Darmstadt, Germany*
[c]*Department Interface Chemistry and Surface Engineering, Max Planck Institute for Sustainable Materials, Max-Planck-Straße 1, 40237 Düsseldorf, Germany*
[d]*Institute for a sustainable Hydrogen Economy (IHE-2), Forschungszentrum Jülich, An der Deutschen Welle 7a, 52428 Jülich, Germany*

This journal is © The Royal Society of Chemistry 2026

Open Access Article. Published on 25 February 2026. Downloaded on 4/22/2026 8:06:35 AM. This article is licensed under a Creative Commons Attribution 3.0 Unported Licence.

OER electrocatalysts in PEM cells due to their high activity, the use of precious metals hinders large-scale applications owing to their scarcity.[19–22] This has driven the search towards OER electrocatalysts based on earth-abundant transition metals. In particular, nickel-, cobalt-, and iron-based materials have emerged as highly active electrocatalysts in alkaline media.[22–26]

Among various oxide phases, these metal-based catalysts can adopt, due to the alkaline conditions, the perovskite structure offers wide compositional variability, stability, and finely tunable properties.[27–30] The general perovskite oxide composition is ABO_3, with A being the larger cation coordinated by 12 oxygen atoms and B being the smaller cation located in corner-sharing oxygen-octahedra. Among the unmixed, first-row transition-metal-based perovskites, $LaNiO_3$ was shown to be one of the most active phases. On the other hand, $LaFeO_3$ is reported to exhibit lower activity.[31–34] $LaNiO_3$ has been extensively studied by Matsumoto *et al.* in pelletized form,[35] by the group of Singh, both coated on Pt foil[36] and Ni supports,[37,38] and by the group of da Silva Pereira coated on Ni foam.[39–41] Furthermore, it is well-reported that the presence of Fe enhances the activity of Ni-based OER electrocatalysts.[42–45] As mixing different cations on either A- or B-site allows for tuning the perovskite properties, it can be reasonably expected that mixing Fe into the B-site of $LaNiO_3$ should exert an activating effect on its ability to catalyze the OER. While $LaNiO_3$ is a metallic conductor[46,47] and $LaFeO_3$ exhibits semiconducting properties,[48] Chiba *et al.* found a conductivity maximum for $LaNi_{1-x}Fe_xO_3$ ($0 \leq x \leq 1$) perovskite phases at about $x = 0.4$.[49] Despite the limited literature on these mixed compositions, some studies, such as those by Zhang *et al.*,[50] Gozzo *et al.*,[51] Bak *et al.*,[52] Yu *et al.*,[53] and Wang *et al.*,[54] report improved OER activity for Fe incorporation levels around or below $x = 0.5$, whereas others, like Hardin *et al.*[55] and Fu *et al.*,[56] found no improvement or slight declines. On the other hand, Adolphsen *et al.*[57] noted increased chemical stability with Fe incorporation, despite unchanged activity.

Despite the interest in perovskites and their potential as electrocatalysts in the OER, their synthesis remains challenging, especially when aiming for enhanced specific surface areas (SSA). Accordingly, simple and cost-effective synthesis methods are crucial for facilitating the large-scale adoption of OER electrocatalysts. High-surface-area materials increase catalyst utilization and electrode–electrolyte contact. Generally, two distinct methods are reported among the few studies on achieving perovskites with high SSAs, with one posing a more extensive method but yielding the highest reported SSAs, and the other being less extensive but yielding lower SSAs in comparison. The first method is nanocasting, where ordered mesoporous carbons or silica, such as SBA-15, are applied as hard templates. Here, depending on the calcination temperature and choice of template, various studies report SSAs, determined from N_2 physisorption following the Brunauer–Emmett–Teller method (S_{BET}), of around 34–130 $m^2\ g^{-1}$ for $LaFeO_3$,[58–60] around 120 $m^2\ g^{-1}$ for $LaMnO_3$,[58] around 97 $m^2\ g^{-1}$ for $LaCoO_3$,[61] and <50 $m^2\ g^{-1}$ for $LaFe_{1-x}Co_xO_3$.[62] The other method involves organic acid-assisted calcination, with studies reporting S_{BET} values in the range of 4–25 $m^2\ g^{-1}$ for $LaNiO_3$,[63] <1–36 $m^2\ g^{-1}$ for $LaM_{1-x}Cu_xO_3$ (M = Mn, Co),[64] and 5–35 $m^2\ g^{-1}$ for $La_{0.8}Sr_{0.2}MO_{3-\delta}$ (M = Mn, Co).[65] Other methods reported for achieving high S_{BET} values include freeze-drying, reaching about 12 $m^2\ g^{-1}$ for $NdCeO_3$,[66] polyethylene glycol complexing, reaching 4–59 $m^2\ g^{-1}$ for $LaMnO_3$,[67] and acid etching as post-treatment, achieving 16–126 $m^2\ g^{-1}$ for $LaMnO_{3+\delta}$.[68] Two studies, reporting the application of high S_{BET} perovskites in the alkaline OER, include syntheses *via* a co-precipitation, with 12–33 $m^2\ g^{-1}$ for $Ln_{0.5}Sr_{0.5}CoO_{3-\delta}$ (Ln = Pr, Nd, Sm, Gd),[69] and de-alloying of arc-melted Al-based alloys, reaching 12 $m^2\ g^{-1}$ for $LaNiO_3$ and 8–20 $m^2\ g^{-1}$ for other $LaMO_3$ phases (M = Co, Mn, Cr).[70] To the best of our knowledge, however, no study employs a facile synthesis yielding perovskite phases based on earth-abundant metals with high SSAs for the application in alkaline OER.

In an earlier work,[71] we reported the application of a synthesis protocol based on the carbon templating route as described by Schwickardi *et al.*[72] to synthesize $LaNi_{1-x}Fe_xO_3$ phases. In the original carbon templating approach, activated carbon was impregnated with an aqueous metal salt precursor solution and then heated in air, simultaneously enabling the calcination of the metal salts to oxides and the removal of the template *via* combustion. However, the direct application of this protocol did not yield the desired $LaNiO_3$ perovskite phase. To address this, we present a modified synthesis protocol here. Following the initial metal salt impregnation and drying steps, the precursor-loaded carbon is additionally impregnated with KOH solution, promoting *in situ* precipitation of metal hydroxides within the porous carbon matrix. Upon thermal treatment, this single-step heating process achieves both the combustion of the carbon template and the conversion of metal hydroxides into the target oxide phases.

Using this refined method, we aimed to synthesize a solid solution series of five lanthanum nickelate/ferrate perovskites with the composition $LaNi_{1-x}Fe_xO_3$ (x = 0.0, 0.25, 0.5, 0.75, and 1.0), which exhibits high SSAs for optimized catalyst utilization for application in the alkaline OER. The resulting materials were comprehensively characterized by powder X-ray diffraction (XRD), scanning electron microscopy (SEM), X-ray photoelectron spectroscopy (XPS), and Raman spectroscopy. Specific surface areas of the powder materials were determined from N_2-physisorption. The elemental composition was obtained from inductively coupled plasma optical emission spectroscopy (ICP-OES). While OER electrocatalysts are commonly applied on highly polished, OER-passive substrates as good testing practice,[18,23,73] different studies hint towards potentially adverse effects and artefacts of such testing methods.[74–76] As such $LaNi_{1-x}Fe_xO_3$ phases have been studied in the OER,[50–57] the focus of this study lies in application-oriented electrode testing to facilitate the large-scale deployment of water electrolysis. Therefore, the electrocatalytic performance of these materials in the OER is evaluated as integral electrodes consisting of ink coatings on industrially relevant nickel substrates, as commonly used in AWE.[13,77]

Open Access Article. Published on 25 February 2026. Downloaded on 4/22/2026 8:06:35 AM. This article is licensed under a Creative Commons Attribution 3.0 Unported Licence.

Experimental

Catalyst preparation

Nickel foil (Alfa Aesar, 0.5 mm thickness, annealed, 99.5%), Ni $(NO_3)_2{\cdot}6H_2O$ (Merck, EMSURE ACS), $La(NO_3)_3{\cdot}6H_2O$ (Sigma-Aldrich, 99.99%), $Fe(NO_3)_3{\cdot}9H_2O$ (Sigma-Aldrich, ≥98%), activated carbon (NORIT CN1, Thermo Scientific), terpineol (Sigma-Aldrich, mixture of isomers), and KOH (Chemsolute, ≥85%) were used as obtained without further purification. Aqueous solutions are prepared with ultra-pure water (Milli-Q). 3400 μL of mixed cation solution was prepared by mixing 1800 μL of aqueous 3 M $La(NO_3)_3$ solution with a total of 1800 μL B-site cation solution, composed of different volumes of aqueous 3 M $Ni(NO_3)_2$ and 3 M $Fe(NO_3)_3$ solution corresponding to the desired Ni/Fe-ratio in the final product. 2.66 g of activated carbon was impregnated with the aqueous mixed cation solution using a pipette. After drying in a desiccator, the carbon was impregnated with 2550 μL of aqueous 6 M KOH solution. After subsequent drying, the impregnated carbon was heated in stagnant air with the following temperature profile: 2 h at 200 °C (5 °C min^{-1} ramp), 2 h at 400 °C (1 °C min^{-1} ramp), and 4 h at 700 °C (3 °C min^{-1} ramp). The resulting powder was washed with deionized (DI) water *via* centrifugation until the supernatant exhibited a neutral pH value. After thorough drying, the resulting powders were ground in an agate mortar.

Catalyst characterization

XRD. The obtained powdered products were measured in a range of 2θ = 10°–90° in 0.02° steps with Cu K_α radiation using a Bruker D2 PHASER XE-T benchtop powder XRD analyzer. Diffraction peak assignment was performed with VESTA version 3.5.8.[78]

SEM images. Electron micrographs were recorded with a COXEM EM30-AXN tabletop SEM from gold-sputtered powder samples using an acceleration voltage of 15 kV in secondary electron detection mode.

N_2 physisorption. After degassing the powder samples at 150 °C for at least 3 h (FloVac degasser), N_2 physisorption isotherms were measured from the powders at −196 °C using a 3P Instruments Quadrasorb SI unit and evaluated using the QuadraWin software. S_{BET} was determined using the Brunauer–Emmett–Teller (BET) method.

ICP-OES. The elemental composition was determined using a SPECTRO Analytical Instruments Spectroblue ICP spectrometer from the products, which were dissolved in concentrated HCl overnight.

XPS. The pristine powder and the catalyst coated before and after CP were investigated using a Thermo Fisher Escalab 250 spectrometer implemented at the DAISY-SOL cluster tool. It is equipped with an Al K_α X-ray source (monochromatic Thermo Fisher XR6, $h\nu$ = 1486.74 eV). Survey and high-resolution spectra were measured in fixed analyzer transmission mode with a pass energy of 50 eV (step size of 0.5 eV) for the survey and 20 eV (step size of 0.05 eV) for the core levels. The system was calibrated to 0.00 eV binding energy of the Fermi level of sputter-cleaned Ag, as well as to the emission lines of Au $4f_{7/2}$ at 83.98 eV, Ag $3d_{5/2}$ at 368.26 eV, and Cu $2p_{3/2}$ at 932.67 eV binding energy with deviations ≤0.1 eV. The data analysis was performed with CasaXPS, version 2.3.22.[79] The core-level spectra were fitted with a Shirley background and peaks of GL(30) line shape. Intensity calculations were done based on relative sensitivity factors published by Scofield.[80] Charge compensation during measurements was achieved using a flood gun, with the voltage carefully adjusted until differential charging effects were corrected. Energy calibration was performed with reference to the C 1s and O 1s peaks.

Raman. The *ex situ* Raman spectra were collected with a LabRAM Raman microscope system (Horiba Jobin Yvon France), using a ×50 objective lens, a 600 l mm^{-1} grating, and a charge-coupled device (CCD) detector. Measurements were performed with a λ = 633 nm helium–neon laser. The incident laser power was about 1 mW focused on a 10 μm^2 sample area, with 3 × 90 s accumulation time and a spectral resolution of about 2 cm^{-1}.

Electrode preparation & measurement

Catalyst inks were prepared by dispersing 200 g L^{-1} catalyst powder in terpineol using an IKA T 10 basic ULTRA-TURRAX homogenizer intermittently for about 3 min, subsequent sonication for 15 min, and vortexing. 1 × 3 cm^2 Ni-sheets were uniaxially polished with SiC-paper (P600 grit, Starcke) in the lengthwise direction and cleaned with DI water and absolute ethanol. Catalyst-coated electrodes were prepared by applying 5 μL of ink to a 1 cm^2 area at the end of the Ni sheet *via* drop-casting, amounting to a catalyst coating density of 1 mg cm^{-2}. The coated Ni sheets were heated in stagnant air for 1 h at 400 °C (10 °C min^{-1} ramp) to remove the terpineol and enhance the mechanical binding of the powder on the Ni substrate. To ensure electrochemical activity only from the coated area, the whole electrode, aside from a few millimeter-wide contacting area at the top (both sides) and the coated area at the bottom, as well as the backside, was insulated with an acrylic spray (Jelt Tropicoat). These electrodes were applied as working electrode (WE) in a three-electrode setup with a 1 × 5 cm^2 glassy carbon (Hochtemperatur Werkstoffe) sheet as counter electrode (CE) at a distance of 15 mm from the WE and a Hg/HgO (1 M KOH, ALS RE-61AP) as reference electrode (RE) in between. All electrochemical measurements were carried out at room temperature with 1 M KOH as electrolyte and recorded with Metrohm Autolab PGSTAT204 potentiostats/galvanostats.

Electrochemical evaluation

All applied or recorded potentials (E_{pstat}) were *iR* drop-corrected and referenced to the reversible hydrogen electrode (RHE) by adding the constant potential of the Hg/HgO (1 M KOH) RE at 0.925 V *vs.* RHE measured against a hydrogen RE (gaskatel Hydroflex) following eqn (3). Here, E_{RHE} is the potential referenced against the RHE, i is the current, and R_u is the uncompensated resistance determined *via* electrochemical impedance spectroscopy (EIS).

$$E_{RHE} = E_{pstat} + 0.925\ V - i \times R_u \quad (3)$$

This journal is © The Royal Society of Chemistry 2026

Open Access Article. Published on 25 February 2026. Downloaded on 4/22/2026 8:06:35 AM.
This article is licensed under a Creative Commons Attribution 3.0 Unported Licence.

For electrochemical evaluation of the samples, the electrodes were initially conditioned by 30 consecutive cyclic voltammograms (CVs) from 0.085 to 1.085 V *vs.* Hg/HgO (1 M KOH) at a scan rate of 100 mV s^{-1}.

Electrochemical activity. For the evaluation of the activity of the coated electrodes, the second forward scan out of two consecutive CVs recorded in a potential window of 0.085 to 1.085 V *vs.* Hg/HgO (1 M KOH) at a scan rate of 5 mV s^{-1} was assessed.

EIS measurements. Impedance spectra were recorded at a potential of 0.685 V *vs.* Hg/HgO with a root mean square perturbation potential amplitude of 10 mV applied for 10 frequencies per decade between 100 kHz and 0.1 Hz. The values of R_u were determined from these measurements.

Chronopotentiometry. For prolonged electrolysis tests, the electrodes were prepared with an additional heating step to further improve catalyst adhesion. After heating in stagnant air at 400 °C, the electrodes were additionally tempered for 3 h at 700 °C (10 K min^{-1}) in a N_2 atmosphere. Initial conditioning was performed with 30 consecutive CVs from −0.515 to 0.285 V *vs.* Hg/HgO (1 M KOH) at a scan rate of 100 mV s^{-1} and five CVs from 0.085 to 1.085 V *vs.* Hg/HgO (1 M KOH) with a 5 mV s^{-1} scan rate. For galvanostatic chronopotentiometry (CP), a constant current density of 10 mA cm^{-2} was applied. Every 4 h, the current was stopped by 30 s of rest (open circuit potential measurement) and one CV from −0.915 to 0.685 V *vs.* Hg/HgO (1 M KOH) at 100 mV s^{-1}. This was repeated six times in total, amounting to a total time of 24 hours of CP.

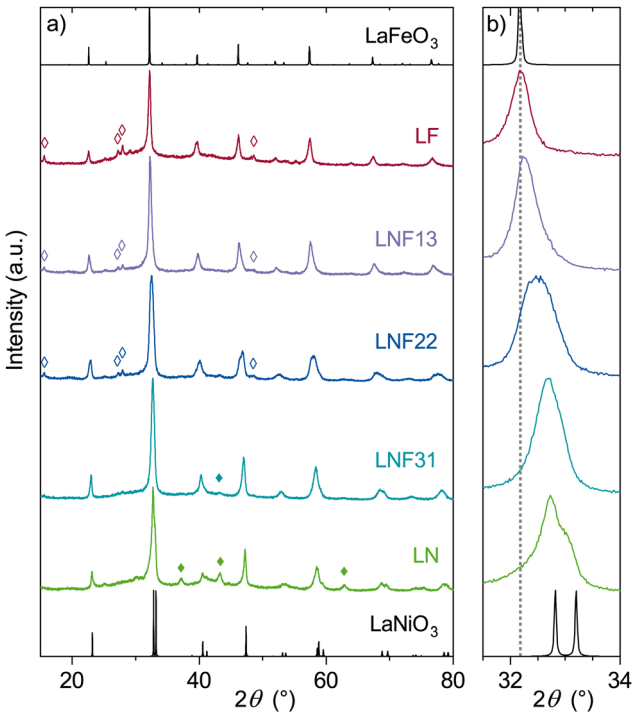

Fig. 1 (a) X-ray diffractograms (XRD) of all $LaNi_{1-x}Fe_xO_3$ samples, including reference diffractograms of $LaNiO_3$ (ICSD-93919) and $LaFeO_3$ (ICSD-28255). Observable secondary phases are marked with ◆ for NiO (ICSD-9866) and with ◊ for $La(OH)_3$ (ICSD-31584). (b) Magnified view of the area between 2θ = 31° and 34°.

Results and discussion

Catalyst characterization

Table 1 lists the abbreviations used for all $LaNi_{1-x}Fe_xO_3$ samples in the following paragraphs. The corresponding XRD patterns of all samples prepared *via* carbon templating are shown in Fig. 1a. Generally, all samples exhibit the perovskite structure as the primary phase, as they show very similar patterns to the reference XRDs of $LaNiO_3$ below and $LaFeO_3$ above, rendered from the inorganic crystal structure database (ICSD).[81] In detail, the XRD diffractogram of LN shows Bragg reflections at 2θ = 23.1°, 40.6°, 47.2°, and 58.7°, which correspond mostly to the (012), (202), (024), and (300) planes of the rhombohedral $LaNiO_3$ phase ($R\bar{3}c$, ICSD-93919[82]). Similarly, the most intense reflections of the LF sample at 2θ = 22.6°, 32.2°, 46.1°, and 57.4° are assigned to the (002), (020/112), (004/220), and (024/132) planes of the orthorhombic $LaFeO_3$ phase (*Pbnm*, ICSD-28255[83]). These reflections can also be found in the LNF31, LNF22, and LNF13 samples.

Table 1 Abbreviations, elemental composition, and specific surface area (S_{BET}) of all prepared $LaNi_{1-x}Fe_xO_3$ samples

Abbrev.	Target composition	La : Ni : Fe-ratio[a]	Estimated composition[b]	S_{BET} (m^2 g^{-1})
LN	$LaNiO_3$	0.9 : 1.0 : 0.0	$LaNi_{0.98}Fe_{0.02}O_3$	69.2
LNF31	$LaNi_{0.75}Fe_{0.25}O_3$	3.9 : 3.2 : 0.9	$LaNi_{0.76}Fe_{0.24}O_3$	43.2
LNF22	$LaNi_{0.5}Fe_{0.5}O_3$	4.0 : 2.1 : 1.8	$LaNi_{0.54}Fe_{0.46}O_3$	61.4
LNF13	$LaNi_{0.25}Fe_{0.75}O_3$	4.1 : 1.1 : 2.8	$LaNi_{0.28}Fe_{0.72}O_3$	61.6
LF	$LaFeO_3$	1.1 : 0.0 : 0.9	$LaFeO_3$	35.8

[a] As determined by ICP-OES. [b] Estimated from ICP-OES-determined elemental composition based on the limiting cation species, assuming stoichiometric parity between A- and B-site cations.

Fig. 1b, which provides a close-up view of the most intense Bragg reflection for each sample, reveals that the main XRD feature of the LN sample at 2θ = 32.7° is shifted slightly to lower 2θ values compared to the reference $LaNiO_3$ (110) plane at 2θ = 32.8°, indicating a slightly enlarged interplanar distance for LN. One possible explanation accounting for the slight downshift of the LN reflection towards lower 2θ values might be a minor presence of Fe, as the estimated phase composition of the LN sample is $LaNi_{0.98}Fe_{0.02}O_3$. The complete metal ratios present in all samples and their estimated perovskite compositions determined from the elemental analysis *via* ICP-OES can be found in Table 1. Assuming complete integration into the perovskite phase, such Fe incorporation would result in enlarged interplanar distances, as the Fe–O distance is larger than the Ni–O distance in the perovskite structure.[82,83] However, as the influence of the minor Fe impurity is expected to be rather negligible, another explanation could be the presence of La-richer Ruddelsden–Popper (RP) perovskite phases with the composition $La_{n+1}Ni_nO_{3n+1}$

Open Access Article. Published on 25 February 2026. Downloaded on 4/22/2026 8:06:35 AM. This article is licensed under a Creative Commons Attribution 3.0 Unported Licence.

(n = 1, 2, 3, ∞). For these phases, the most intense reflection shifts from $LaNiO_3$ (n = ∞) with decreasing n towards lower 2θ values.[84] *E.g.*, an orthorhombic $La_4Ni_3O_{10}$ (*Cmca*, ICSD-96720,[85] n = 3) exhibits its most intense reflection at 2θ = 32.2° (171). Due to this proximity of the reflections, the overlay of XRD patterns, resulting from the presence of any RP phase along with $LaNiO_3$, would be expected to shift the most intense reflection in LN towards lower 2θ values.

Generally, a consecutive downshift of the main Bragg reflection with higher Fe content from LN to the LF sample can be observed (Fig. 1b), indicating the successful synthesis of the $LaNi_{1-x}Fe_xO_3$ perovskite solid-solution series with both Ni and Fe on the B-site.

However, all samples show additional reflections corresponding to secondary phases present. Such features can be found for LN at 2θ = 37.2°, 43.3°, and 62.9°, corresponding to the (111), (200), and (220) planes of a cubic NiO phase ($Fm\bar{3}m$, ICSD-9866 [86]). For LNF31, only a very weak reflection at 2θ = 43.3° of the NiO (200) plane is visible. On the other hand, LNF22, LNF13, and LF show reflections at 2θ = 15.7°, 27.3°, 28.0°, and 48.7° that can be attributed to the (100), (110), (101), and (300) planes of a hexagonal $La(OH)_3$ phase ($P6_3/m$, ICSD-31584 [87]). As detected by ICP-OES and listed in Table 1, the metal ratios correlate well with these secondary phases. LN and LNF13 feature an excess of Ni, which results in the formation of NiO after calcination. Likewise, LNF22, LNF13, and LF feature an excess of La, apparently resulting in the formation of $La(OH)_3$. One possible explanation for the detected metal ratios deviating from the desired ones could lie in the calcination and combustion of the impregnated carbon. Schwickardi *et al.* report a catalyzed combustion of carbon in the presence of metal species.[72] Furthermore, the well-researched combustion of soot is reported to be catalyzed to varying degrees by different metal–oxide species. Among the three metals involved in this study, Fe exhibits the highest ratio, followed by La, and the lowest catalytic soot combustion activity is found for Ni.[88,89] Thus, it could be expected that metals with higher catalytic rates get dragged out more during the carbon combustion step in the oven, leaving less Fe than La and less La than Ni in the samples, resulting in the formation of NiO and $La(OH)_3$ excess phases. Nonetheless, the XRD and ICP-OES results indicate that the perovskite synthesis procedure was successful overall, as indicated by the comparably low presence of secondary phases and the closely matching sample stoichiometries.

The impregnation synthesis method was chosen to produce particles with high surface areas, thereby allowing for an increased catalyst utilization through an enlarged electrode–electrolyte interface. N_2 physisorption should allow for a precise determination of the specific surface areas S_{BET} of powders and is applied here for all samples. The values listed in Table 1 indeed show high S_{BET} values for all perovskite compositions, spanning from 35.8 $m^2\ g^{-1}$ for LF to 69.2 $m^2\ g^{-1}$ for LN, which ranges above the typically reported S_{BET} values for high SSA-perovskites prepared by comparably facile syntheses such as organic acid-assisted calcination or co-precipitation.[63–65,69] However, a nearly twofold spread appears unexpected for materials of similar molecular weights synthesized by the same method. Furthermore, the S_{BET} values lack a clear trend. A determination of the residual carbon content in the samples amounts to below 1 wt%, indicating mostly a successful combustion of the templating carbon. However, as the activated carbon exhibits a large specific surface area, even such small amounts left in the sample will strongly influence the surface areas of the samples determined by N_2 physisorption and, thus, explain the wide spread of the S_{BET} values. The complete N_2 physisorption isotherms can be found in Fig. S1.

Scanning electron micrographs (SEM) were then recorded to visually assess the effect of the synthesis method on the surface structure. Exemplarily, the SEM images of LN (Fig. 2a and b) and LF (Fig. 2c and d) are shown, with further SEM images for all samples depicted in Fig. S2–S6. Here, the particles appear without regular or uniform shape and exhibit a wide size distribution, ranging from the nm scale to more than 100 μm for larger agglomerates. Furthermore, the particles appear very rugged and flaky, exhibiting surface features over many orders of magnitude. Such intense surface roughness can, in turn, account for the relatively high S_{BET} values, conforming to the main objective of the activated carbon templating method.

The X-ray photoelectron spectra (XPS) recorded from the powder samples are shown in Fig. 3. It is well-established that the La $3d_{3/2}$ peak overlaps with the Ni $2p_{3/2}$ peak, complicating

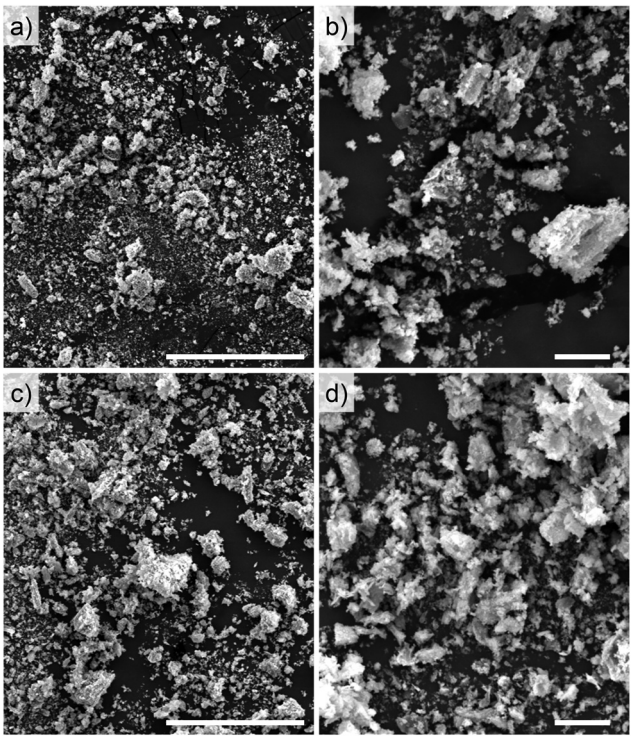

Fig. 2 Scanning electron micrographs of (a) and (b) $LaNiO_3$ as well as (c) and (d) $LaFeO_3$. Scale bars: (a) and (c) 100 μm, (b) and (d) 10 μm.

 This journal is © The Royal Society of Chemistry 2026

Open Access Article. Published on 25 February 2026. Downloaded on 4/22/2026 8:06:35 AM.
This article is licensed under a Creative Commons Attribution 3.0 Unported Licence.

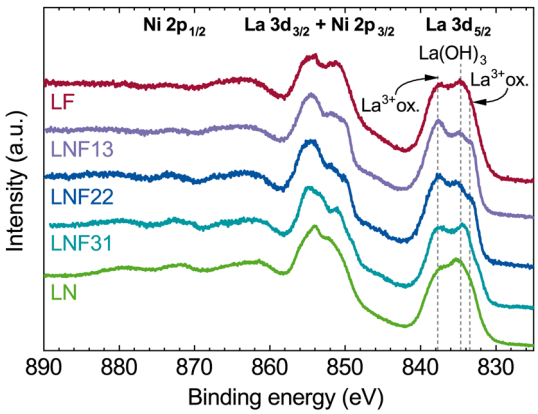

Fig. 3 XPS binding energies of La 3d and Ni 2p core-level spectra of all powder $LaNi_{1-x}Fe_xO_3$ samples. The La $3d_{5/2}$ area shows three peaks corresponding to $La(OH)_3$ and the $3d_{5/2}$ core level and satellite of the oxidic La(III) species (La^{3+} ox.) in the perovskites.

spectral interpretation.[90] The most intense Ni $2p_{3/2}$ signal is typically accompanied by a satellite feature located approximately 6–7 eV higher in binding energy.[91,92] Notably, this satellite component coincides with the plasmon loss feature of the La $3d_{3/2}$ core level, further contributing to the overlap.[93] Thus, accurate analysis of the Ni $2p_{3/2}$ core-level spectra is not feasible without concurrently considering the La $3d_{3/2}$ region. The intrinsic complexity of the La $3d_{3/2}$ spectral structure significantly complicates deconvolution and precise profiling of the Ni $2p_{3/2}$ signal.

Nonetheless, the XPS binding energy of the La $3d_{5/2}$ core level at approximately 833.5 eV, along with its multiplet splitting or charge transfer band near 837.7 eV, is consistent with the presence of La(III) species in the perovskite phase. An additional La $3d_{5/2}$ peak at 834.7 eV can be attributed to $La(OH)_3$, which aligns with previously reported data.[94,95] Unlike the XRD results, however, the XPS data reveal the presence of $La(OH)_3$ in every sample, suggesting the formation of surface-level $La(OH)_3$ in each case. Due to the overlap of Ni $2p_{3/2}$ and La $3d_{3/2}$ signals, a clear distinction between Ni(II) and Ni(III) species is not possible. However, the Ni $2p_{1/2}$ core level at 873 eV confirms the presence of Ni(II) species. While XRD analysis shows NiO as a secondary phase in LN and LNF31, the weak Ni $2p_{1/2}$ signal observed in LNF22 suggests the presence of surface-level $Ni(OH)_2$ in the Ni-rich samples.

Additionally, Fig. S7 shows the Ni 3p and Fe 3p core-level spectra in the 45–80 eV region, revealing a clear trend of decreasing Ni 3p and increasing Fe 3p signal intensity with increasing Fe content. The relative amounts of Ni and Fe (Table S1), calculated from the integrated Ni 3p and Fe peak areas and corrected by the appropriate relative sensitivity factors (RSFs), show higher Ni contents than those determined by ICP-OES. This discrepancy might indicate surface Fe depletion. However, considering the relatively low signal intensity, the resulting uncertainty in the Ni/Fe ratios, and the overall different sensitivity of each method, the XPS-derived Ni/Fe contents are roughly consistent with the ICP-OES-determined bulk compositions (Table 1). The Ni 3p spectra indicate a dominant Ni(II) contribution, while the expected shifts toward higher binding energy associated with Ni(III) are not clearly resolved. Given the extent of differential charging and signal noise, fitting the Ni 3p peaks was avoided to prevent introducing arbitrary interpretations. Although bulk $LaNiO_3$ nominally is expected to contain Ni(III), surface states may deviate significantly from this stoichiometry. Furthermore, the presence of RP phases, as indicated by XRD analysis, would also contribute to a small portion of Ni(II) present in the bulk material.

The Raman measurements of the powder samples yielded only weak responses. Therefore, the $LaNi_{1-x}Fe_xO_3$ perovskite phases are characterized by Raman spectra recorded from coatings on Ni substrates, as shown in Fig. 4. For the LF sample, the collected Raman signal is consistent with literature results on $LaFeO_3$.[96] On the other hand, LN shows a relatively weak and broad feature at about 410 cm^{-1}, assignable to the strongest Raman feature of $LaNiO_3$.[97] Possible reasons for the weak Raman signal might involve the metallic nature of LN, as well as small crystallite sizes, which contribute to its broader XRD reflections.

Overall, the Raman response intensity of the $LaNi_{1-x}Fe_xO_3$ solid solution series remains weak, with additional features appearing for different samples. In particular, LNF31 exhibits two broad Raman bands at about 400 and 560 cm^{-1}, attributed to Ni–O and Fe–O stretching vibrations. Increasing the Fe content further to LNF22 results in an additional peak at 470 cm^{-1}, while another feature appears at 650 cm^{-1} in LNF13, consistent with a gradual replacement of Ni with Fe in the perovskite lattice. Notably, no $La(OH)_3$-related Raman vibrations were observed in any sample,[98] indicating overall concentrations below the Raman spectroscopic resolution. Furthermore, no Raman signal is expected for NiO. However, defective NiO_x or $Ni(OH)_2$ might yield a Raman band close to 450 cm^{-1},[99] which would strongly overlap with the recorded $LaNi_{1-x}Fe_xO_3$ Raman signals.

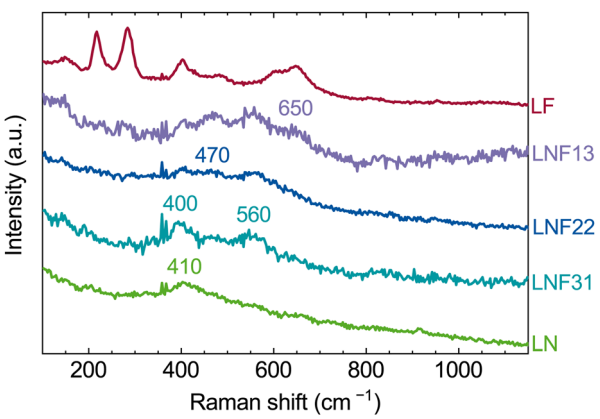

Fig. 4 Raman spectra for all $LaNi_{1-x}Fe_xO_3$ samples coated on Ni substrates recorded at λ = 633 nm and a temperature of 300 K.

Open Access Article. Published on 25 February 2026. Downloaded on 4/22/2026 8:06:35 AM. This article is licensed under a Creative Commons Attribution 3.0 Unported Licence.

Evaluation of the electrochemical performance

The perovskite powder samples were coated as inks onto Ni substrates to evaluate the OER performance in 1 M KOH electrolyte. The electrode surface was conditioned with 30 consecutive CVs from 1.0 to 2.0 V *vs.* the reversible hydrogen electrode (RHE). To determine the electrochemical OER activity, two CVs in the same potential window before *iR* drop-correction, reaching into the OER overpotential region, were then recorded, with the second forward scan considered. One representative scan from triplicate measurements for each sample is shown in Fig. 5. At low potentials, only very low currents are detected for all samples, and thus, no chemical reaction occurs. For such potential sweeps, the electrochemical activity can be directly linked to the current. Hence, higher current densities (j) at lower potentials equal higher activity. Therefore, the absence of current at applied potentials significantly above 1.23 V correlates with the high activation barrier of the OER.

The inset of Fig. 5 shows small oxidation peaks at about 1.37 V *vs.* RHE for all samples, which can be attributed to the oxidation of Ni(II) to Ni(III) species,[42,100,101] with similar behavior reported for $LaNiO_3$ coated on different Ni substrates by the groups of Singh[37,38] and da Silva Pereira.[39–41] It can be expected that the B-site cations in these $La^{3+}Ni_{1-x}^{3+}Fe_x^{3+}O_3^{2-}$ phases are already in the oxidation state of +3. Thus, a Ni(II)/Ni(III)-oxidation peak should, in principle, not arise from the Ni in the perovskite structure, aside from small amounts of Ni(II)-containing secondary phases present in LN and LNF31. Further possibilities for the presence of this oxidation couple could be oxygen deficiency in the perovskite phase, as reported by Matsumoto *et al.*,[35] which requires Ni(II) species present for electrical neutrality, or RP phases with lower n values, which also contain Ni(II) species. However, the intensity of this oxidation peak does not correlate with the Ni content in the catalyst coatings, especially since the Ni-free LF-coated sample shows one of the largest peak areas. Therefore, it is plausible that the Ni-substrate itself and not the perovskite might cause the oxidation peak evidenced in the CV. While the coatings appear visibly dense, it is expected that the electrolyte comes in contact with the Ni-substrate at possible coating imperfections at the edges, as well as penetrating the coating between its constituent particles. The smaller peak area of LN in comparison to the other samples could, therefore, be accounted for by a denser coating layer, leaving less direct contact between the electrolyte and the Ni-substrate. Indeed, SEM images of the coated electrodes (as shown in Fig. S8 and S9 for LN and LF) reveal a notable difference in the surface structure. While LN exhibits a much denser surface with only a few pores and cracks, the surface of the LF-coated electrode does not appear as homogeneous, with individual particles clumped together, thereby allowing for many pores and gaps in between.

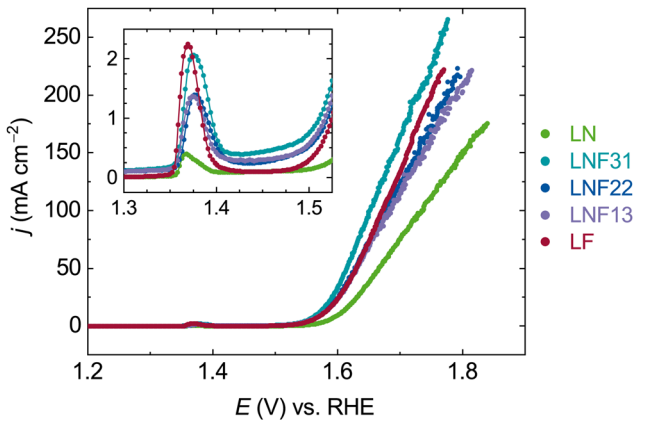

Fig. 5 *iR* drop-corrected forward scans of cyclic voltammograms of all perovskite-coated Ni-electrodes measured in 1 M KOH at a scan rate of 5 mV s^{-1} against a Hg/HgO (1 M KOH) reference electrode and glassy carbon counter electrode. One representative CV forward from three electrodes per composition. Inset with magnification in the area of 1.3 and 1.5 V *vs.* RHE shows oxidation peaks.

At about 1.5 V *vs.* RHE, the increase in current density indicates the onset of the OER, with LNF31, LNF22, LNF13, and LF showing lower onset potentials than LN. As all samples exhibit high perovskite phase purity, the electrocatalysis of the OER can be assumed to follow the OER mechanisms discussed in the literature as reported elsewhere.[27,54,102–104] Generally, the mechanisms on perovskites mainly evolve around the d orbitals of the B cation, following the conventional adsorbate evolution mechanism (AEM), or for higher B–O covalency, following the lattice oxygen mechanism (LOM).[98–100]

Upon further potential increase, all samples exhibit different rates of current density rise. In this representative measurement, the highest current density is reached for LNF31 at 265 mA cm^{-2}. Almost equal current densities of about 222 mA cm^{-2} are found for LF, LNF22, and LNF31, but at increasing potentials in that order. As prior to *iR*-correction, the same potentials were applied, the difference in potentials at the maximum currents mainly derives from the difference in uncompensated resistances. LN exhibits the lowest maximum current of about 176 mA cm^{-2} at the highest overpotentials. Interestingly, the least active sample LN exhibits the smallest Ni(II)/Ni(III) oxidation peak area, suggesting a significant influence of the coating porosity and, thus, accessibility of the electrolyte to the Ni substrate on the activity. The order of these peak sizes is roughly reflected in the activities.

A key benchmarking value commonly used to quantify and compare the activity of OER-electrocatalysts is the overpotential η, which is defined as the additional potential required to reach a specific current density relative to the OER equilibrium potential of 1.23 V *vs.* RHE. The overpotentials necessary to reach a current density of 10 mA cm^{-2} for all samples are shown in Fig. 6, with the mean and error values determined from triplicate measurements. Here, the significantly lower activity of LN compared to all other samples is clearly evidenced by its visibly higher overpotential of 398 ± 20 mV, which is about 60 mV higher than that of LNF31, with the second-highest overpotential. LNF31, LNF22, and LNF13 exhibit very similar overpotentials of 340 ± 8, 334 ± 10, and 335 ± 8 mV, respectively. Additionally, LF, as the most active

 This journal is © The Royal Society of Chemistry 2026

Open Access Article. Published on 25 February 2026. Downloaded on 4/22/2026 8:06:35 AM. This article is licensed under a Creative Commons Attribution 3.0 Unported Licence.

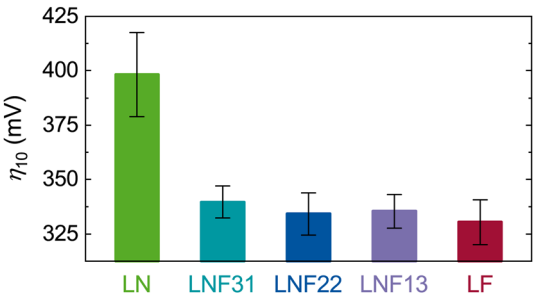

Fig. 6 Overpotentials η_{10} of all samples determined at a current density of 10 mA cm^{-2} during CV forward scans recorded with 5 mV s^{-1}, averaged over three measured electrodes per composition.

sample with an overpotential of 330 ± 11 mV, does not reach significantly lower overpotentials compared to the other Fe-containing samples. Hence, the Ni/Fe ratio only marginally influences the OER activity of the tested $LaNi_{1-x}Fe_xO_3$ perovskite phases.

An increase in activity with the introduction of Fe to Ni-based OER electrocatalysts, and thus, an activity increase from LN to LNF31, is expected from literature reports.[50–52] These studies find different optimal Fe-contents on the B-site of $LaNi_{1-x}Fe_xO_3$ phases, but all concur on values below x = 0.5. Similarly, optima of Fe contents in NiFe oxyhydroxide OER electrocatalysts were found between 10 and 50% with only minimal activity difference within this range.[105] Therefore, the similar activity of LNF31 and LNF22 can also be expected. However, the higher electrocatalytic OER activity for samples with Fe-content above x = 0.5 is most surprising, as different reports state a lower activity for $LaFeO_3$ compared to $LaNiO_3$,[31,34,106] and thus, LF would be presumed to exhibit a higher overpotential than LN.

While not offering an extensive explanation, the aforementioned difference in coating density, illustrated by the differently sized Ni(II)/Ni(III) oxidation peaks and substantiated by the SEM images of the coated electrodes (Fig. S8 and S9), could influence the current density, as only the geometric area of the electrode is accounted for. These coating differences indicate a significantly larger surface area for catalysts with high Fe contents, which could compensate for their expected intrinsically lower OER activity. Nonetheless, it should also be considered here that LNF22 and LNF13 feature significantly smaller oxidation peaks but exhibit similar activity compared to LF. Furthermore, these overpotentials do not correlate linearly with the corresponding integrated Ni(II)/Ni(III) oxidation peak areas marked in Fig. S10a, as shown in Fig. S10b. Therefore, the coating density does not fully explain the trend in activity shown in Fig. 6.

Furthermore, the significantly lower activity of LN compared to all other samples might result from the suspected presence of RP phases in LN, as described in the respective XRD analysis. Studies by Yu *et al.*, Cao *et al.*, and Choi *et al.* concurrently report decreasing alkaline OER activity with decreasing n in the $La_{n+1}Ni_nO_{3n+1}$ RP phases.[107–109] Thus, the presence of any RP phase in LN would be expected to lower the OER activity of LN. Additional electrochemical characterization is provided by the Tafel plots presented in Fig. S11, from which the Tafel slopes were calculated, as listed in Table S2. Here, all samples exhibit rather similar values, which roughly correspond to a literature reported value for $LaNiO_3$.[33] These Tafel slopes indicate similar kinetic behavior between the different samples. Thus, the observed activity differences most likely result from different limitations throughout the porous catalyst coating and on the oxidised substrates surface.[110,111] Furthermore, electrochemical impedance spectroscopy (EIS) measurements can be found in the Nyquist plots depicted in Fig. S12. Here, the impedance spectra were recorded in the same measurement as the CVs shown in Fig. 3 and reflect a similar trend in charge transfer resistances estimated from the width of the half-circle-like course in the Nyquist plot.

Electrochemical stability. For prolonged electrolysis at a constant current, the coated electrodes were additionally tempered in a pure N_2 atmosphere for 3 h at 700 °C to increase the mechanical adhesion of catalyst particles, as the coating method is not optimized for longer durations of electrolysis. Thus, detachment of the catalyst is occasionally observed after prolonged contact with the electrolyte while stirring. Furthermore, the electrolysis was paused every four hours to remove gas bubbles that could potentially block the electrode. The course of the galvanostatic chronopotentiometry (CP) at an applied current density of 10 mA cm^{-2} in 1 M KOH at room temperature for all samples during 24 h is shown in Fig. 7.

Initially, all samples require a higher starting potential to reach 10 mA cm^{-2} than the overpotential η_{10} shown in Fig. 6. This most likely results from the additional tempering step, which could partially lead to electrode passivation, as well as from compaction of the coating layer through sintering, which in turn would decrease the active surface area. Fig. S13 shows SEM images of the coatings of LN and LF after this additional sintering step. While LN does not exhibit any observable

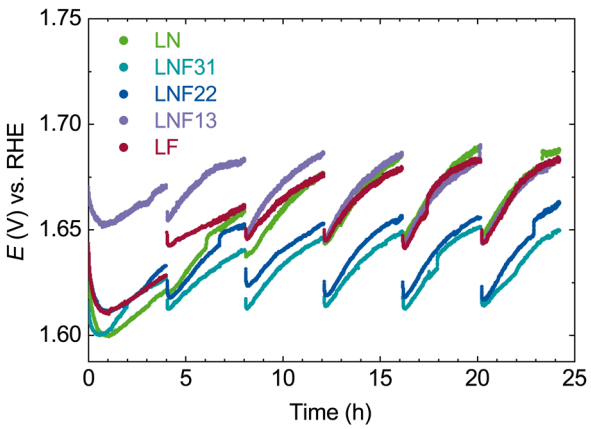

Fig. 7 Galvanostatic chronopotentiometry at 10 mA cm^{-2} interrupted every 4 h. Jumps in potential can be attributed to detachment of gas bubbles and refilling of ultra-pure water to compensate for the decrease in electrolyte volume through electrolysis and condensation.

Open Access Article. Published on 25 February 2026. Downloaded on 4/22/2026 8:06:35 AM.
This article is licensed under a Creative Commons Attribution 3.0 Unported Licence.

changes, the surface of the LF-coated samples shows significant changes, as it reveals a denser surface with less distinguishable individual particles compared to the LF coating before N_2 tempering. Interestingly, all samples exhibit a decrease in potential and, thus, activation to varying degrees in the first hour, followed by an increase in potential, which equals deactivation in the subsequent hours. After each interruption, the samples show activation again, albeit much less pronounced than in the first hour, followed by stronger deactivation. During the first eight hours, the potentials of all samples reach higher values than at the beginning. Thereafter, however, most samples appear to stabilize, exhibiting a constant cycle of deactivation for four hours and an equal degree of regained activity after CP interruption, demonstrating the almost complete reversibility of the deactivation occurring during the four-hour CP interval.

Each sample, however, shows a different course of CP. While LNF13 starts at the highest potential of about 1.67 V *vs.* RHE and remains the least active sample within the first eight hours, it is the only sample that exhibits a lower potential right after the second interruption compared to the minimum in the first four-hour period. Furthermore, LNF13 does not exhibit a pronounced overall deactivation but rather a high constancy, as the degree of deactivation remains largely constant after the initial four hours. The second-highest starting potential of about 1.64 V *vs.* RHE is found for LF and LNF22, which is higher than that of LN. This could be explained by the stronger coating sintering effect observed for the samples containing high Fe contents, as shown in Fig. S14. LF shows a strong deactivation with the first interruption, not restoring but further deactivating the electrode. On the other hand, the deactivation of LNF22 is less intense and, like LNF13, shows a high constancy with almost no increase in deactivation after four hours. While the lowest initial starting potentials of 1.63 and 1.62 V *vs.* RHE are found for LN and LNF31, respectively, LN exhibits the highest amount of relative deactivation as it reaches high potentials similar to LF and LNF13 during the CP, and also features low constancy as it is the only sample with further potential increase after 8 h. During the CP measurement, LNF31 appears to be the most active and stable sample, with only a little increase in potential.

At the end of the 24 h, LN, LNF13, and LF exhibit the highest potential of about 1.68 V *vs.* RHE and, thus, show the lowest activity during this duration of electrolysis. The more active and stable samples, LNF22 and LNF31, reach lower potentials of 1.66 and 1.65 V *vs.* RHE after 24 h. Interestingly, this OER activity trend after 24 h of CP at 10 mA cm^{-2} is much closer to the expected trend reported in the literature. Specifically, LNF31 and LNF22 exhibit a significantly increased OER activity compared to LN upon the introduction of Fe contents of $x \leq 0.5$, whereas a decreased activity for Fe contents above $x > 0.5$ (LNF13 and LF) compared to LNF31 and LNF22 is observed. However, the potentials of LF remain equal and do not surpass LN, in contrast to literature reports.

XPS analyses were performed on the coated electrodes before and after 24 h of CP. Representative data in Fig. 8 show

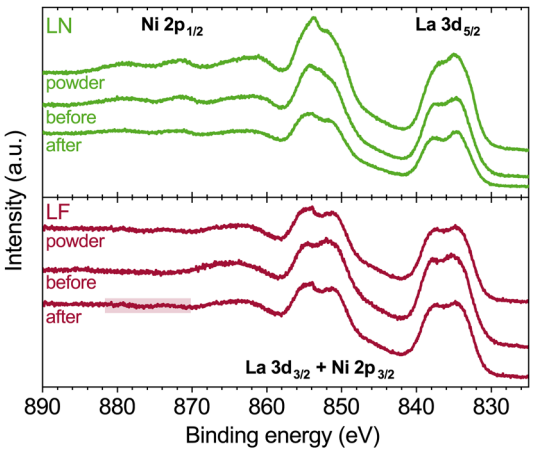

Fig. 8 XPS binding energies of La 3d and Ni 2p core-level spectra of LN and LF as powder and as catalyst coating on Ni substrate before and after galvanostatic chronopotentiometry at 10 mA cm^{-2} for 24 h in 1 M KOH electrolyte.

the Ni 2p and La 3d core-level spectra of LN and LF compared to their respective powder XPS. LN does not exhibit significant spectral changes following the coating process or CP, indicating chemical stability. In contrast, LF displays a weak Ni $2p_{1/2}$ peak after CP, suggesting the presence of Ni(II) species in the Ni-free LF-coated sample. The complete comparison of Ni 2p and La 3p core-level spectra before and after CP, shown in Fig. S13, reveals only minor differences across all samples, supporting the chemical stability of the perovskite coatings during CP. The chemical and structural stability of the perovskite samples is further supported by a comparison of the Raman spectra before and after CP, as shown in Fig. S15, with observable signal reduction most likely induced by mechanical loss of catalyst particles. The Ni 3p and Fe 3p core-level spectra of all samples before and after CP are shown in Fig. S16. The Ni and Fe fractions calculated from the integrated peak areas, listed in Table S3, confirm that the compositions remain largely unchanged following the coating process—though the relatively low signal intensities lead to large margins of error.

However, the Ni 3p and Fe 3p core-level spectra recorded after CP reveal significant amounts of Ni in the Fe-rich LNF13 and LF samples, as listed in Table S3. Representative SEM images of the LN- and LF-coated electrodes recorded after 24 h of CP (Fig. S17) depict many holes in the catalyst coating, measuring about tens of micrometers. These holes contain little to no catalyst inside, revealing the bare Ni substrate below. Such holes could be attributed to a mechanical loss of catalyst material during 24 h of CP under constant stirring, with oxygen gas evolving in the pre-existing cracks and openings in the coating layer, potentially detaching loosely bound catalyst particles. This loss of catalyst material also explains the overall observed deactivation of all samples during 24 h of CP, underlining the importance of resilient coating methods. The high Ni contents detected by XPS analysis after CP most likely result from the previously covered, and thus undetectable, Ni substrate in the holes. This effect is more pronounced for samples with

This journal is © The Royal Society of Chemistry 2026

Open Access Article. Published on 25 February 2026. Downloaded on 4/22/2026 8:06:35 AM. This article is licensed under a Creative Commons Attribution 3.0 Unported Licence.

higher Fe contents, especially LNF13 and LF. Also, the electrolyte-accessible surface of the Ni substrate has most likely oxidized through the tempering steps and the CP, accounting for the observable Ni $2p_{1/2}$ peak for the LF sample after CP.

Conclusions

A solid solution series of $LaNi_{1-x}Fe_xO_3$ perovskite phases was prepared by a modified carbon templating method, where activated carbon is impregnated with metal nitrate precursors, which are precipitated by a second impregnation step with KOH. Subsequent heating enables the removal of the template through combustion and calcination towards the desired phases, as confirmed by XRD analysis, and substantiated by XPS and Raman spectroscopy. SEM images and N_2 physisorption attest to high surface areas, which are equal to or higher than commonly reported for similarly facile syntheses. In contrast to literature-reported trends, high Fe content catalysts exhibit higher OER activity in 1 M KOH electrolyte, potentially due to less dense and more porous coatings, as exemplified by coated $LaFeO_3$. Chronopotentiometry for 24 h at 10 mA cm^{-2} displays different degrees of deactivation for all samples, which most likely could be attributed to catalyst coating detachment, as XPS comparison of the coated samples before and after CP indicates chemical stability of the perovskite phases. In conclusion, this work provides a foundation for further investigation of lanthanum nickelate/ferrates coated on nickel substrates as anodes in large-scale alkaline water electrolysis applications.

Author contributions

Nikolas M. Kubo: writing – original draft, writing – review & editing, conceptualization, methodology, investigation, visualization, Harol M. Fernández: writing – review & editing, investigation, Ilias Efthimiopoulos: writing – review & editing, investigation, Leila Novalic: investigation, Martin Rabe: writing – review & editing, methodology, supervision, funding acquisition, Jan P. Hofmann: writing – review & editing, supervision, funding acquisition, and Regina Palkovits: writing – review & editing, conceptualization, methodology, supervision, funding acquisition.

Conflicts of interest

The authors declare that they have no known competing financial interests or personal relationships that could have appeared to influence the work reported in this paper.

Data availability

The majority of the data supporting this article, including XRD, N_2 physisorption, and all electrochemical data will be made available after manuscript acceptance on Zenodo.

Supplementary information is available. See DOI: https://doi.org/10.1039/d5nr05003k.

Acknowledgements

We gratefully acknowledge the German Federal Ministry of Research, Technology and Space (BMFTR) for providing financial support within the H_2Giga cluster project PrometH_2eus (FKZ: 03HY105A, 03HY105H and 03HY105J). We also thank Noah Avraham-Radermacher for the XRD measurements and Heike Bergstein for the ICP-OES measurements.

References

1 M. Momirlan and T. N. Veziroglu, *Int. J. Hydrogen Energy*, 2005, **30**, 795–802.
2 N. Mac Dowell, N. Sunny, N. Brandon, H. Herzog, A. Y. Ku, W. Maas, A. Ramirez, D. M. Reiner, G. N. Sant and N. Shah, *Joule*, 2021, **5**, 2524–2529.
3 G. Marbán and T. Valdés-Solís, *Int. J. Hydrogen Energy*, 2007, **32**, 1625–1637.
4 M. Ball and M. Wietschel, *Int. J. Hydrogen Energy*, 2009, **34**, 615–627.
5 A. M. Oliveira, R. R. Beswick and Y. Yan, *Curr. Opin. Chem. Eng.*, 2021, **33**, 100701.
6 N. Sazali, *Int. J. Hydrogen Energy*, 2020, **45**, 18753–18771.
7 N. Armaroli and V. Balzani, *ChemSusChem*, 2011, **4**, 21–36.
8 A. Buttler and H. Spliethoff, *Renewable Sustainable Energy Rev.*, 2018, **82**, 2440–2454.
9 T. E. Mallouk, *Nat. Chem.*, 2013, **5**, 362–363.
10 S. Wang, A. Lu and C.-J. Zhong, *Nano Convergence*, 2021, **8**, 4.
11 M. El-Shafie, *Results Eng.*, 2023, **20**, 101426.
12 S. A. Grigoriev, V. N. Fateev, D. G. Bessarabov and P. Millet, *Int. J. Hydrogen Energy*, 2020, **45**, 26036–26058.
13 J. Brauns and T. Turek, *Processes*, 2020, **8**, 248.
14 M. A. Khan, H. Zhao, W. Zou, Z. Chen, W. Cao, J. Fang, J. Xu, L. Zhang and J. Zhang, *Electrochem. Energy Rev.*, 2018, **1**, 483–530.
15 P. Millet, Fundamentals of water electrolysis, in *Electrochemical power sources: fundamentals, systems, and applications:Hydrogen production by water electrolysis*, ed. T. Smolinka and J. Garche, Elsevier, Amsterdam, Oxford, Cambridge, MA, 2022, pp. 37–62.
16 H. Dau, C. Limberg, T. Reier, M. Risch, S. Roggan and P. Strasser, *ChemCatChem*, 2010, **2**, 724–761.
17 S. Anwar, F. Khan, Y. Zhang and A. Djire, *Int. J. Hydrogen Energy*, 2021, **46**, 32284–32317.
18 C. C. L. McCrory, S. Jung, I. M. Ferrer, S. M. Chatman, J. C. Peters and T. F. Jaramillo, *J. Am. Chem. Soc.*, 2015, **137**, 4347–4357.
19 T. Wang, X. Cao and L. Jiao, *Carbon Neutrality*, 2022, **1**, 21.
20 S. Trasatti, *J. Electroanal. Chem. Interfacial Electrochem.*, 1980, **111**, 125–131.

Open Access Article. Published on 25 February 2026. Downloaded on 4/22/2026 8:06:35 AM. This article is licensed under a Creative Commons Attribution 3.0 Unported Licence.

21 Y. Matsumoto and E. Sato, *Mater. Chem. Phys.*, 1986, **14**, 397–426.
22 C. C. L. McCrory, S. Jung, J. C. Peters and T. F. Jaramillo, *J. Am. Chem. Soc.*, 2013, **135**, 16977–16987.
23 M. Yu, E. Budiyanto and H. Tüysüz, *Angew. Chem., Int. Ed.*, 2022, **61**, e202103824.
24 J. R. Galán-Mascarós, *ChemElectroChem*, 2015, **2**, 37–50.
25 F. Lyu, Q. Wang, S. M. Choi and Y. Yin, *Small*, 2019, **15**, e1804201.
26 M.-I. Jamesh and X. Sun, *J. Power Sources*, 2018, **400**, 31–68.
27 J. Hwang, R. R. Rao, L. Giordano, Y. Katayama, Y. Yu and Y. Shao-Horn, *Science*, 2017, **358**, 751–756.
28 M. A. Peña and J. L. Fierro, *Chem. Rev.*, 2001, **101**, 1981–2017.
29 A. S. Bhalla, R. Guo and R. Roy, *Mater. Res. Innovations*, 2000, **4**, 3–26.
30 X. Xu, W. Wang, W. Zhou and Z. Shao, *Small Methods*, 2018, **2**, 1800071.
31 I. C. Man, H.-Y. Su, F. Calle-Vallejo, H. A. Hansen, J. I. Martínez, N. G. Inoglu, J. Kitchin, T. F. Jaramillo, J. K. Nørskov and J. Rossmeisl, *ChemCatChem*, 2011, **3**, 1159–1165.
32 J. O. Bockris and T. Otagawa, *J. Phys. Chem.*, 1983, **87**, 2960–2971.
33 J. O. Bockris and T. Otagawa, *J. Electrochem. Soc.*, 1984, **131**, 290–302.
34 J. Suntivich, K. J. May, H. A. Gasteiger, J. B. Goodenough and Y. Shao-Horn, *Science*, 2011, **334**, 1383–1385.
35 Y. Matsumoto, H. Yoneyama and H. Tamura, *J. Electroanal. Chem. Interfacial Electrochem.*, 1977, **80**, 115–121.
36 R. N. Singh, L. Bahadur, J. P. Pandey, S. P. Singh, P. Chartier and G. Poillerat, *J. Appl. Electrochem.*, 1994, **24**, 149–156.
37 R. N. Singh, S. K. Tiwari, S. P. Singh, A. N. Jain and N. K. Singh, *Int. J. Hydrogen Energy*, 1997, **22**, 557–562.
38 S. P. Singh, R. N. Singh, G. Poillearat and P. Chartier, *Int. J. Hydrogen Energy*, 1995, **20**, 203–210.
39 C. O. Soares, M. D. Carvalho, M. E. Jorge, A. Gomes, R. A. Silva, C. M. Rangel and M. I. Pereira, *Port. Electrocim. Acta*, 2011, 335–342.
40 C. O. Soares, M. D. Carvalho, M. E. Melo Jorge, A. Gomes, R. A. Silva, C. M. Rangel and M. I. da Silva Pereira, *J. Appl. Electrochem.*, 2012, **42**, 325–332.
41 C. O. Soares, R. A. Silva, M. D. Carvalho, M. M. Jorge, A. Gomes, C. M. Rangel and M. I. da Silva Pereira, *Electrochim. Acta*, 2013, **89**, 106–113.
42 D. A. Corrigan, *J. Electrochem. Soc.*, 1987, **134**, 377–384.
43 L. Trotochaud, J. K. Ranney, K. N. Williams and S. W. Boettcher, *J. Am. Chem. Soc.*, 2012, **134**, 17253–17261.
44 L. Trotochaud, S. L. Young, J. K. Ranney and S. W. Boettcher, *J. Am. Chem. Soc.*, 2014, **136**, 6744–6753.
45 S. Anantharaj, S. Kundu and S. Noda, *Nano Energy*, 2021, **80**, 105514.
46 J. B. Goodenough and P. M. Raccah, *J. Appl. Phys.*, 1965, **36**, 1031–1032.
47 W. T. Hong, K. A. Stoerzinger, Y.-L. Lee, L. Giordano, A. Grimaud, A. M. Johnson, J. Hwang, E. J. Crumlin, W. Yang and Y. Shao-Horn, *Energy Environ. Sci.*, 2017, **10**, 2190–2200.
48 T. Arima, Y. Tokura and J. B. Torrance, *Phys. Rev. B: Condens. Matter Mater. Phys.*, 1993, **48**, 17006–17009.
49 R. Chiba, F. Yoshimura and Y. Sakurai, *Solid State Ionics*, 1999, **124**, 281–288.
50 D. Zhang, Y. Song, Z. Du, L. Wang, Y. Li and J. B. Goodenough, *J. Mater. Chem. A*, 2015, **3**, 9421–9426.
51 C. B. Gozzo, M. R. Soares, J. C. Sczancoski, I. C. Nogueira and E. R. Leite, *Int. J. Hydrogen Energy*, 2019, **44**, 21659–21672.
52 J. Bak, T. G. Yun, J.-S. An, H. B. Bae and S.-Y. Chung, *Energy Environ. Sci.*, 2022, **15**, 610–620.
53 N. Yu, H.-J. Liu, Y.-N. Cao, Q.-Y. Wang, Y. Ma, J.-F. Yu, H. Hu, Y.-M. Chai and B. Dong, *Colloids Surf., A*, 2022, **654**, 130042.
54 L. Wang, P. Adiga, J. Zhao, W. S. Samarakoon, K. A. Stoerzinger, S. R. Spurgeon, B. E. Matthews, M. E. Bowden, P. V. Sushko, T. C. Kaspar, G. E. Sterbinsky, S. M. Heald, H. Wang, L. W. Wangoh, J. Wu, E.-J. Guo, H. Qian, J. Wang, T. Varga, S. Thevuthasan, Z. Feng, W. Yang, Y. Du and S. A. Chambers, *Nano Lett.*, 2021, **21**, 8324–8331.
55 W. G. Hardin, J. T. Mefford, D. A. Slanac, B. B. Patel, X. Wang, S. Dai, X. Zhao, R. S. Ruoff, K. P. Johnston and K. J. Stevenson, *Chem. Mater.*, 2014, **26**, 3368–3376.
56 G. Fu, W. Li, J.-Y. Zhang, M. Li, C. Li, N. Li, Q. He, S. Xi, D. Qi, J. L. MacManus-Driscoll, J. Cheng and K. H. Zhang, *Small*, 2021, **17**, e2006930.
57 J. Q. Adolphsen, B. R. Sudireddy, V. Gil and C. Chatzichristodoulou, *J. Electrochem. Soc.*, 2018, **165**, F827–F835.
58 S. Afzal, X. Quan and J. Zhang, *Appl. Catal., B*, 2017, **206**, 692–703.
59 J. Zhao, Y. Liu, X. Li, G. Lu, L. You, X. Liang, F. Liu, T. Zhang and Y. Du, *Sens. Actuators, B*, 2013, **181**, 802–809.
60 H. Su, L. Jing, K. Shi, C. Yao and H. Fu, *J. Nanopart. Res.*, 2010, **12**, 967–974.
61 Y. Wang, J. Ren, Y. Wang, F. Zhang, X. Liu, Y. Guo and G. Lu, *J. Phys. Chem. C*, 2008, **112**, 15293–15298.
62 R. de Lima, M. S. Batista, M. Wallau, E. A. Sanches, Y. P. Mascarenhas and E. A. Urquieta-González, *Appl. Catal., B*, 2009, **90**, 441–450.
63 M. El Baydi, S. K. Tiwari, R. N. Singh, J.-L. Rehspringer, P. Chartier, J. F. Koenig and G. Poillerat, *J. Solid State Chem.*, 1995, **116**, 157–169.
64 P. Porta, S. de Rossi, M. Faticanti, G. Minelli, I. Pettiti, L. Lisi and M. Turco, *J. Solid State Chem.*, 1999, **146**, 291–304.
65 Y. Teraoka, H. Kakebayashi, I. Moriguchi and S. Kagawa, *J. Alloys Compd.*, 1993, **193**, 70–72.
66 A. González, E. Martínez Tamayo, A. Beltrán Porter and V. Cortés Corberán, *Catal. Today*, 1997, **33**, 361–369.

 This journal is © The Royal Society of Chemistry 2026

Open Access Article. Published on 25 February 2026. Downloaded on 4/22/2026 8:06:35 AM. This article is licensed under a Creative Commons Attribution 3.0 Unported Licence.

67 G. Zou, Z. Wang, M. Sun, X. Luo and X. Wang, *J. Nat. Gas Chem.*, 2011, **20**, 294–298.
68 B. Zhao, R. Ran, L. Sun, X. Guo, X. Wu and D. Weng, *RSC Adv.*, 2016, **6**, 69855–69860.
69 C. Hwang, O. Gwon, H. Jo, K. M. Ok and G. Kim, *ChemElectroChem*, 2017, **4**, 468–471.
70 C. Si, C. Zhang, J. Sunarso and Z. Zhang, *J. Mater. Chem. A*, 2018, **6**, 19979–19988.
71 N. M. Kubo, R. Mhamdi and R. Palkovits, *Fuel Cells*, 2024, **24**, e202300239.
72 M. Schwickardi, T. Johann, W. Schmidt and F. Schüth, *Chem. Mater.*, 2002, **14**, 3913–3919.
73 C. Wei, R. R. Rao, J. Peng, B. Huang, I. E. L. Stephens, M. Risch, Z. J. Xu and Y. Shao-Horn, *Adv. Mater.*, 2019, **31**, e1806296.
74 T. Lazaridis, B. M. Stühmeier, H. A. Gasteiger and H. A. El-Sayed, *Nat. Catal.*, 2022, **5**, 363–373.
75 S. Geiger, O. Kasian, A. M. Mingers, S. S. Nicley, K. Haenen, K. J. J. Mayrhofer and S. Cherevko, *ChemSusChem*, 2017, **10**, 4140–4143.
76 H. A. El-Sayed, A. Weiß, L. F. Olbrich, G. P. Putro and H. A. Gasteiger, *J. Electrochem. Soc.*, 2019, **166**, F458–F464.
77 D. E. Hall, *J. Electrochem. Soc.*, 1981, **128**, 740–746.
78 K. Momma and F. Izumi, *J. Appl. Crystallogr.*, 2011, **44**, 1272–1276.
79 N. Fairley, V. Fernandez, M. Richard-Plouet, C. Guillot-Deudon, J. Walton, E. Smith, D. Flahaut, M. Greiner, M. Biesinger, S. Tougaard, D. Morgan and J. Baltrusaitis, *Appl. Surf. Sci. Adv.*, 2021, **5**, 100112.
80 J. H. Scofield, *J. Electron Spectrosc. Relat. Phenom.*, 1976, **8**, 129–137.
81 D. Zagorac, H. Müller, S. Ruehl, J. Zagorac and S. Rehme, *J. Appl. Crystallogr.*, 2019, **52**, 918–925.
82 J. C. Park, D. K. Kim, S. H. Byeon and D. Kim, *J. Synchrotron Radiat.*, 2001, **8**, 704–706.
83 M. Marezio and P. D. Dernier, *Mater. Res. Bull.*, 1971, **6**, 23–29.
84 Y. Adachi, N. Hatada, K. Hirota, M. Kato and T. Uda, *J. Am. Ceram. Soc.*, 2019, **102**, 7077–7088.
85 V. I. Voronin, I. F. Berger, V. A. Cherepanov, L. Gavrilova, A. N. Petrov, A. I. Ancharov, B. P. Tolochko and S. G. Nikitenko, *Nucl. Instrum. Methods Phys. Res., Sect. A*, 2001, **470**, 202–209.
86 S. Sasaki, K. Fujino and Y. Takéuchi, *Proc. Jpn. Acad., Ser. B*, 1979, **55**, 43–48.
87 W. H. Zachariasen, *Acta Crystallogr.*, 1948, **1**, 265–268.
88 J. P. A. Neeft, M. Makkee and J. A. Moulijn, *Appl. Catal., B*, 1996, **8**, 57–78.
89 B. Stanmore, J. Brilhac and P. Gilot, *Carbon*, 2001, **39**, 2247–2268.
90 *Handbook of X-ray photoelectron spectroscopy – A reference book of standard spectra for identification and interpretation of XPS data*, ed. J. F. Moulder and J. Chastain, Perkin-Elmer Corporation, 1992, update.
91 J. F. Marco, J. R. Gancedo, M. Gracia, J. L. Gautier, E. I. Ríos, H. M. Palmer, C. Greaves and F. J. Berry, *J. Mater. Chem.*, 2001, **11**, 3087–3093.
92 H. C. Siegmann, L. Schlapbach and C. R. Brundle, *Phys. Rev. Lett.*, 1978, **40**, 972–975.
93 C. Suzuki, J. Kawai, M. Takahashi, A.-M. Vlaicu, H. Adachi and T. Mukoyama, *Chem. Phys.*, 2000, **253**, 27–40.
94 V. Celorrio, E. Dann, L. Calvillo, D. J. Morgan, S. R. Hall and D. J. Fermin, *ChemElectroChem*, 2016, **3**, 283–291.
95 Lanthanum spectra – La metal – lanthanum metal, https://xpsdatabase.net/lanthanum-spectra-la-metal-lanthanum-metal, (accessed June 2025).
96 B. Jiang, L. Li, Q. Zhang, J. Ma, H. Zhang, K. Yu, Z. Bian, X. Zhang, X. Ma and D. Tang, *J. Mater. Chem. A*, 2021, **9**, 13008–13018.
97 N. Chaban, M. Weber, S. Pignard and J. Kreisel, *Appl. Phys. Lett.*, 2010, **97**, 031915.
98 S. R. Sanivarapu, J. B. Lawrence and G. Sreedhar, *ACS Omega*, 2018, **3**, 6267–6278.
99 H. Moreno Fernández, A. Alkemper, K. Wang, C. Jr. Mempin, J. Gallenberger and J. P. Hofmann, *J. Catal.*, 2024, **440**, 115823.
100 S. L. Medway, C. A. Lucas, A. Kowal, R. J. Nichols and D. Johnson, *J. Electroanal. Chem.*, 2006, **587**, 172–181.
101 M. Alsabet, M. Grdeń and G. Jerkiewicz, *Electrocatalysis*, 2015, **6**, 60–71.
102 L.-B. Liu, C. Yi, H.-C. Mi, S. L. Zhang, X.-Z. Fu, J.-L. Luo and S. Liu, *Electrochem. Energy Rev.*, 2024, **7**, 14.
103 H. Sun, J. Dai, W. Zhou and Z. Shao, *Energy Fuels*, 2020, **34**, 10547–10567.
104 J. T. Mefford, X. Rong, A. M. Abakumov, W. G. Hardin, S. Dai, A. M. Kolpak, K. P. Johnston and K. J. Stevenson, *Nat. Commun.*, 2016, **7**, 11053.
105 F. Dionigi and P. Strasser, *Adv. Energy Mater.*, 2016, **6**, 1600621.
106 A. Ashok, A. Kumar, R. R. Bhosale, F. Almomani, S. S. Malik, S. Suslov and F. Tarlochan, *J. Electroanal. Chem.*, 2018, **809**, 22–30.
107 J. Yu, J. Sunarso, Y. Zhu, X. Xu, R. Ran, W. Zhou and Z. Shao, *Chem. – Eur. J.*, 2016, **22**, 2719–2727.
108 C. Cao, C. Shang, X. Li, Y. Wang, C. Liu, X. Wang, S. Zhou and J. Zeng, *Nano Lett.*, 2020, **20**, 2837–2842.
109 S. R. Choi, J.-I. Lee, H. Park, S. W. Lee, D. Y. Kim, W. Y. An, J. H. Kim, J. Kim, H.-S. Cho and J.-Y. Park, *Chem. Eng. J.*, 2021, **409**, 128226.
110 V. Briega-Martos, R. Guzman-Soriano, J. Jiang and Y. Yang, *Nat. Catal.*, 2025, **8**, 863–866.
111 O. van der Heijden, S. Park, R. E. Vos, J. J. J. Eggebeen and M. T. M. Koper, *ACS Energy Lett.*, 2024, **9**, 1871–1879.